THE JOURNAL OF PHYSICAL CHEMISTRY A
A JOURNAL OF THE AMERICAN CHEMICAL SOCIETY

pubs.acs.org/JPCA Article

Electronic Relaxation Dynamics in 2-Quinolinones with Extended Conjugation

Published as part of The Journal of Physical Chemistry virtual special issue "Daniel Neumark Festschrift".

Alana Fligelman, Gonto Johns, Christina Guyn, Alexis Petrauskas, Paul A. Vadola, and Graham B. Griffin*

Cite This: *J. Phys. Chem. A* 2021, 125, 9757–9769 Read Online

ACCESS | Metrics & More | Article Recommendations | Supporting Information

ABSTRACT: The 2-quinolinone family of molecules, also known as carbostyrils, have been proposed as light absorbing donor molecules in energy transfer based sensing schemes and as possible photocatalysts. Both of these applications make use of electronic excited states, but the photophysics of 2-quinolinones have not yet been examined closely. This study applies static and dynamic spectroscopy, with supporting density functional theory calculations, to reveal the electronic relaxation dynamics of a family of five 2-quinolinones with extended conjugated rings. These modifications lead to red-shifted absorbance and emission maxima, relative to unmodified 2-quinolinone. Optical excitation of these molecules with near UV light resulted in transitions with strong $\pi \rightarrow \pi^*$ and HOMO → LUMO character. Time-correlated single photon counting measurements yielded fluorescence lifetimes ranging from 849.3 (±0.6) ps to 4.586 (±0.002) ns. Transient absorption spectroscopy revealed relaxation dynamics of the S_1 excited state formed by photoexcitation at 350 nm, along with formation of a long-lived signal assigned as excited state absorption by a triplet excited state. Vibrational relaxation in the S_1 state was also characterized in some compounds. Overlapping signals of S_1 decay and triplet growth in the transient absorption data set could not be fully disentangled. These results demonstrate a highly competitive relaxation scheme following multiple simultaneous pathways, a promising situation for establishing chemical control of electronic relaxation in the 2-quinolinone family.

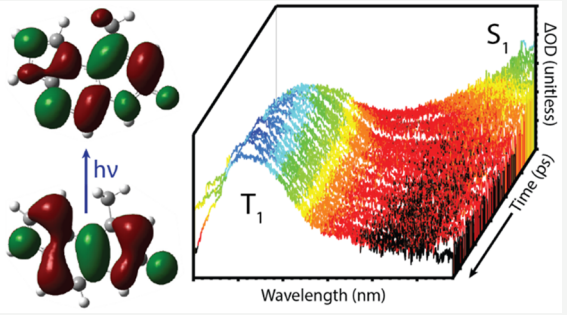

1. INTRODUCTION

Quinolinones have been proposed as potential drugs for treatment of cancers,[1−4] in addition to other medical applications.[5−11] They have also been explored as high-energy antennae for fluorescence resonance energy transfer (FRET) and luminescence resonance energy transfer (LRET) measurements,[12−16] and as anchoring groups in dye-sensitized solar cells.[17] Additionally, the photochemical synthesis of quinolinone derivatives has received significant attention.[18,19] The correlation of structure and function is critical in all of these applications, and outside of medical applications the behavior electronic excited states is of particular interest.

The 2-quinolinone family of molecules, also known as carbostyrils, are used in photosensing and other optical applications.[20−22] Despite their common use, the photophysics of 2-quinolinones have not received as much attention as the closely related coumarin family[23] (see Figure 1). The 2-quinolinones offer higher energy absorbance and emission features than the coumarins, as well as enhanced chemical and thermal stability, and less sensitivity to pH. Coumarins exhibit higher fluorescence quantum yield than 2-quinolinones, and their optical properties are more chemically tunable.[24] A substantial library of 2-quinolinones has been characterized by static absorption and emission spectroscopy,[25−27] leading to rational design of molecules with lower energy absorbance and emission features.[28] Fluorescence lifetimes and quantum yields have also been characterized in commercially available 2-

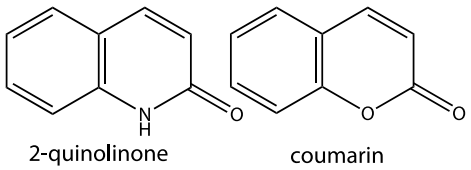

Figure 1. Coumarins and 2-quinolinones have very closely related structures. Coumarins are lactones, while 2-quinolinones contain a lactam ring.

Received: May 24, 2021
Revised: October 11, 2021
Published: November 4, 2021

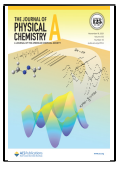

https://doi.org/10.1021/acs.jpca.1c04560
J. Phys. Chem. A 2021, 125, 9757–9769

quinolinones,[29] showing that the relaxation of electronic excited states in 2-quinolinones proceeds through a different pathway than that observed in coumarins. More recently, vibrationally resolved fluorescence measurements of a jet-cooled 2-quinolinone confirmed little structural variation between the electronic ground state structure and the S_1 excited state structure.[30]

Detailed dynamic measurements of electronic relaxation, subsequent to photoexcitation, have been examined in the context of the development of FRET[31,32] and LRET[16,33,34] sensing schemes, where 2-quinolinones perform well as light absorbers paired with high-yield emitters. These studies focused on the performance of the sensing scheme as a whole, rather than looking specifically at electronic relaxation in the 2-quinolinones themselves. Still, dynamic measurements presented as part of these studies revealed fluorescence lifetimes of a few nanoseconds in 2-quinolinones, with energy transfer efficiencies of up to 50% when paired in an optimized donor−acceptor scheme.[35] In comparison to coumarins, 2-quinolinones have been noted to exhibit sharper optical transitions with more well-defined vibronic features, leading to smaller Stokes shifts.[36]

Measurements of electronic relaxation dynamics in 2-quinolinones have also been presented, in the context of a cyclobutane-based dimer photoreversion reaction.[37] Transient absorption (TA) measurements were performed on a 7-methoxy-1-methylquinolin-2(1*H*)-one monomer in acetonitrile solution, revealing subpicosecond relaxation to the lowest energy singlet excited state. Singlet excited state lifetimes of a few hundred picoseconds were reported, along with formation of a triplet excited state with a lifetime of 70 ns under aerobic conditions. This triplet lifetime increased to 500 ns in deoxygenated solution. This result highlights a key difference between 2-quinolinones and the more popular coumarin family, a significant yield of triplet excited state population following photoexcitation via the lowest energy absorption features.

Quinolinones have also been recently identified as photoreactive substrates[38] and photocatalysts.[39] The mechanisms of these processes have not yet been studied in sufficient detail to determine the relative importance of various electronic relaxation pathways or reveal any structure−function relationships.

Here we present a detailed study of electronic relaxation dynamics in a series of chemically modified 2-quinolinones, selected from a group of molecules recently synthesized via the gold-catalyzed hydroarylation of *N*-aryl alkynamides.[40] The relationship between chemical structure and optical properties was closely examined using a combination of static spectroscopy and computational chemistry. Dynamic spectroscopy was applied to quantitatively track electronic relaxation dynamics after photoexcitation. The goal of this study is to determine how chemical structure impacts these relaxation dynamics. We aim to identify aspects of the structure of 2-quinolinones (Figure 2) that can be tuned to enhance desirable optical properties or be used to direct photochemistry and photocatalysis.

2. METHODS

2.1. Experimental Methods. The 2-quinolinone molecules studied here were supplied by the Vadola group, and the compounds were synthesized following their previously published methods.[40]

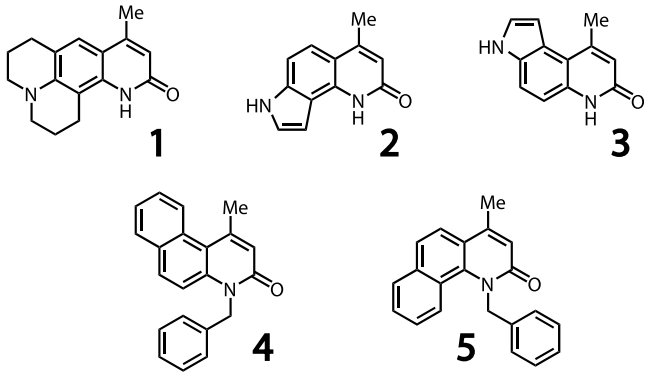

Figure 2. The structure of the five 2-quinolinone molecules selected for this study are diagrammed. Each molecule is based on a 2-quinolinone core, with ring structures extended in various ways. All molecules also include a methyl group at the 4 position on the quinolinone rings.

Absorbance spectra of each compound in methanol solution were recorded on a Cary 100 UV Vis spectrometer. Emission spectra in methanol solution were acquired on a Cary Eclipse fluorescence spectrometer. UV-compatible, 1 cm path length quartz cuvettes were used for both measurements, which were recorded at 1 nm intervals at room temperature. All spectra were recorded at multiple concentrations to confirm linearity with concentration. ACS certified ≥99.8% methanol solvent was purchased from Fisher Scientific.

TA spectra were recorded in 2 mm path length cuvettes, at optical densities near 0.2. A HELIOS femtosecond TA spectrometer from Ultrafast Systems was employed. Ultrafast laser pulses were generated by a Spectra-Physics Tsunami oscillator and amplified with a Spitfire Pro amplifier. Frequency conversion was accomplished via a TOPAS-C optical parametric amplifier and subsequent frequency conversion in BBO crystals. Samples were pumped at 350 nm, with 400 μW of power, at a repetition rate of 2.5 kHz. Probe pulses generated by focusing the 800 nm laser fundamental into sapphire were used to record spectra over the accessible detection range of the instrument, 425−750 nm. The time delay between pump and probe pulses was introduced with a computer-controlled mechanical delay stage. The instrument time resolution was ∼50 fs, and the accessible time range was ∼2.6 ns. No evidence of photodamage to the samples or buildup of photoproducts during the measurements was observed in sequentially measured spectra.

The TA data set was analyzed by multiexponential fitting of transient kinetics, and also by global rate analysis. To fit transient kinetics, wavelength ranges representing each spectral feature were selected by inspection, the data within the range was integrated at each time delay, and then the resulting kinetic traces were fitted to a multiexponential model. Data acquired at time delays less than 3 ps were excluded from fitting to prevent distortion of the kinetic fits by the large number of data points recorded at these early times, because subpicosecond dynamics were not the focus of this analysis. The specific wavelength ranges integrated for each compound are shown in the Supporting Information, along with fitting results.

To perform global rate analysis,[41] data was first preprocessed using Surface Xplorer 4.3.0 software. The data set was cropped to the 425−750 nm wavelength range, corresponding to the stable region of the probe spectrum. Each data set was then

https://doi.org/10.1021/acs.jpca.1c04560
J. Phys. Chem. A 2021, 125, 9757−9769

baseline corrected via subtraction of the average of 8−10 featureless spectra acquired at negative time delays. Transient spectra containing invalid measurements within the 425 nm −750 nm wavelength range were then replaced by interpolation of neighboring spectra. Global rate analysis was then performed using Glotaran 1.5.1 software. All models employed a Gaussian instrument response function, which fit to an average value of 46.7 (±0.3) fs. All models also employed a third order polynomial accounting for dispersion, and a function accounting for coherent artifacts found at early time delays. The number of kinetic components included in each model varied depending on the compound. Each kinetic component in a global analysis model is associated with an exponential decay time constant, and also both a decay associated difference spectrum (DADS) and an evolution associated difference spectrum (EADS). The DADS for a kinetic component is the spectrum of fitted amplitudes associated with the exponential decay process, while the EADS reports directly on the changes in the transient spectrum over time. These spectra may or may not correspond well with the species associated difference spectrum (SADS), which is the spectrum of an initial, intermediate, or final state of the sample being probed. Both sequential and parallel decay schemes were investigated. Results of all models are reported in the Supporting Information. Because the TA data sets for all compounds contain a feature that does not decay during the observed time domain, the longest time constant in all models was fixed to a pseudoinfinite value of 10^{10} ps. The strategy of fixing a second time constant to the S_1 lifetime value measured via time-correlated single photon counting (TCSPC) was also explored. Reported uncertainties in time constants are standard errors from the global rate analysis fitting procedure. For all models discussed, residuals were examined and found not to contain significant remaining signal. These residuals are available as Supporting Information.

The TCSPC measurements of fluorescence lifetimes were recorded with a ChronosBH time-domain fluorometer. Samples were prepared in methanol solution, with concentrations near 1×10^{-5} M. A 345 nm, 10 MHz LED light source was used for excitation, and the spectral window for detection was set with a 50 nm bandpass filter centered at 445 nm. Time constants were extracted from TCSPC data by first fitting the instrument response, measured using scattered light from a LUDOX colloidal silica solution, to a Gaussian function. The standard deviation of the fitted Gaussian function was 0.7897 (±0.0006) ns. The TCSPC data was then fitted to a convolution of this Gaussian function and a single exponential decay, with Gaussian parameters fixed to the values from the initial fit of the instrument response. Reported uncertainties in decay time constants are standard errors from the fitting procedure. All data sets fit to single exponential decays, with residuals showing no significant remaining signal. All fits and residuals are available as Supporting Information.

2.2. Computational Methods. Computational electronic structure results were obtained by first preoptimizing the geometry of each molecule with the semiempirical PM6 method and then reoptimizing the resulting structures with density functional theory (DFT). The CAM-B3LYP functional and the 6-31G(d,p) basis set were used for all DFT calculations. All calculations included the methanol solvent by applying the polarizable continuum model. Once the optimized structures were determined, the structures were verified as energy minima through frequency calculations that yielded only positive frequencies for all vibrational modes. The optimized structures were then used in additional calculations required to build energy level diagrams. The vertical detachment energies were determined, so that the S_0 energy levels could be compared on a common energy axis. To obtain vertical detachment energies, the optimized ground state geometries were used to calculate the energy of the molecule as a monovalent cation, with doublet spin multiplicity. The resulting energies were compared to the ground state neutral singlet energy at the same geometry to determine the vertical electron detachment energy of each molecule. The first 10 singlet excited states of each neutral molecule were also calculated, using time-dependent density functional theory (TDDFT) and applying the same functional and basis set as the ground state calculations. Singlet excited state energy levels were then determined by adding the calculated excited state transition energies to the energy of the optimized neutral ground state. Finally, the energy of the lowest triplet excited state of each neutral molecule was calculated at the ground state geometry. All calculations were performed using the Gaussian 16 software package.[42]

To aid in assignment of the features found in the TA data sets, the geometry of each compound was also optimized in the S_1 state with TDDFT calculations, using the same approach employed for the ground state geometry. The result of each structural optimization was verified as an energy minimum with a corresponding frequency calculation, and then excited states of each compound were recalculated at the S_1 geometry using TDDFT. Comparing the energies of these excited states resulted in predictions of the $S_1 \rightarrow S_n$ transition energies, used to assign excited state absorption features in the TA data sets. A similar set of calculations was attempted for the lowest energy triplet state of each compound, but the structural optimizations failed to converge on an energy minimum.

3. RESULTS AND DISCUSSION

3.1. Absorbance Spectra and Electronic Structure Calculations. Five 2-quinolinones with extended conjugation networks were selected from the library of available compounds.[40] Optimized ground state singlet geometries are shown in Figure 3. All five molecules preserved the planar, conjugated region of the 2-quinolinone while extending the structure through additional ring-fusions to the benzo-ring of the 2-quinolinone core. As a result of the common method of synthesis, all five structures also have a methyl group at the 4 position on the quinolinone rings. In **1** the quinolinone ring was fused to the benzo-ring of julolidine, yielding a tetracyclic compound. The amino-nitrogen atom of the julolidine core was coplanar with the original quinolinone ring and part of both saturated rings, but the remainder of the rings were based on sp^3 carbons that break planarity and conjugation. In **2** and **3**, the planar and conjugated region of the molecules extended over an added pyrrole ring. In **2** the pyrrole ring was closer to nitrogen atom in the lactam ring, connecting at the 7 and 8 positions of the quinolinone moiety, while in **3** the connection was made at the 5 and 6 positions and the pyrrole was further from the lactam's nitrogen atom. Molecules **4** and **5** both extended the planar and conjugated quinolinone structure through an added benzene ring. This addition was made in two positions, analogous to the addition of the pyrrole ring in **2** and **3**, with **4** adding the benzyl ring farther from the lactam's nitrogen atom and the added ring in **5** being closer to the nitrogen atom. Molecules **4** and **5** also included a pendant

https://doi.org/10.1021/acs.jpca.1c04560
J. Phys. Chem. A 2021, 125, 9757−9769

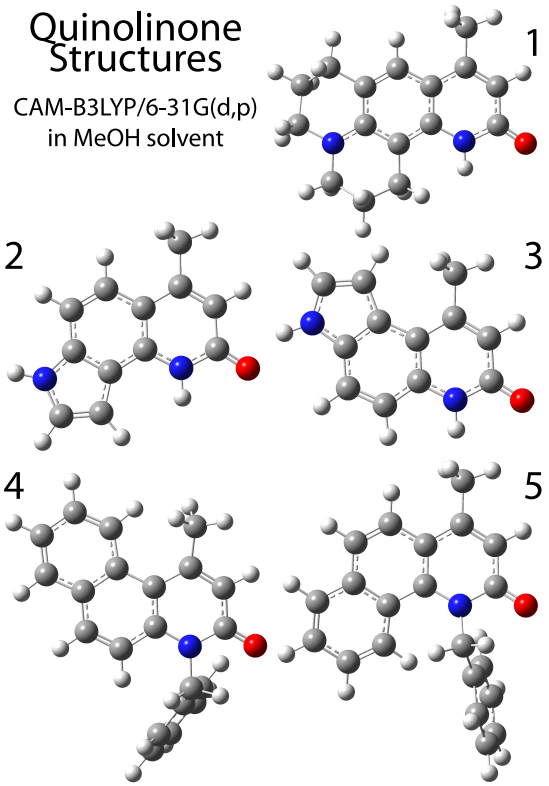

Figure 3. The structure of each molecule in its electronic ground state was preoptimized with semiempirical methods, then reoptimized with DFT using the CAM-B3LYP functional and the 6-31G(d,p) basis set. Methanol solvent was included via the polarizable continuum model. The atoms in the structures are color coded as C (gray), H (white), N (blue), and O (red). All optimized structures were verified as energy minima with frequency calculations that returned positive frequency values for all normal modes.

benzyl group bound to the nitrogen atom in the lactam. This group was itself planar and conjugated, but it was not coplanar with the quinolinone moiety or included in its conjugation network.

The absorbance spectra of compounds **1**–**5** in methanol solution are shown in Figure 4. Molar absorptivity maxima of the lowest-energy absorbance peaks, appearing near 350 nm, were observed in the range $(0.5–2.0) \times 10^4$ M^{-1} cm^{-1}. Slightly larger absorbance values were observed in higher energy peaks, with molar absorptivity still falling below 6×10^4 M^{-1} cm^{-1}. Molecules with closely related structures, the pair **2**, **3** and the pair **4**, **5**, showed absorbance features at similar energies and with similar shapes. All compounds were found to have lowest-energy peaks red-shifted from 2-quinolinone, which has been reported to have an absorbance maximum at 327.9 nm in methanol solution.[26] In the cited study, the peak absorbance wavelength in methanol solution was not reported for 4-methylquinolin-2(1*H*)-one, which also contains the additional methyl group found in compounds **1**–**5**. A value of 331 nm was reported in dimethyl sulfoxide (DMSO) solvent for this compound. Several similar compounds were examined in both DMSO and methanol solution, including unsubstituted 2-quinolinone. The lowest-energy absorbance maxima were observed to blueshift by 500–800 cm^{-1} when the solvent was changed from DMSO to methanol. The effect of solvent on the absorption and emission features of various substituted 2-quinolinones has been previously characterized.[24,26,27] For the compounds most similar to those studied here, a blueshift of the absorbance maxima by ∼800 cm^{-1} was reported as the solvent dielectric constant increased from a value of ∼2 for *n*-hexane solution to a value of ∼79 for aqueous solution. Both protic and aprotic solvents followed this same trend, although DMSO was a consistent exception yielding lower energy absorption maxima despite a high dielectric constant. In aqueous solution, the emission maximum of the related molecule 4-cyanocarbostyril was observed to be independent of pH over the pH = 1–11 range.

Closer inspection of the lowest-energy absorbance features of compounds **1**–**5** reveals additional patterns. Molecule **1** was observed to have both the most red-shifted and the strongest absorbance, peaking at 375 nm. This result was unexpected, because **1** has the smallest coplanar, conjugated moiety of any compound studied. The lowest-energy absorbance of closely related molecules **2** and **3** peaked near 340 nm, and both spectra had broad lineshapes with slight shoulder peaks that may indicate unresolved vibronic progressions. Molecule **3** had a slightly broader peak, extending ∼10 nm farther toward long wavelengths. The other closely related pair of molecules, **4** and **5**, also showed very similar absorbance features. The longest wavelength feature appeared in the 350–370 nm range for these molecules. Both compounds yielded a two-peak vibronic

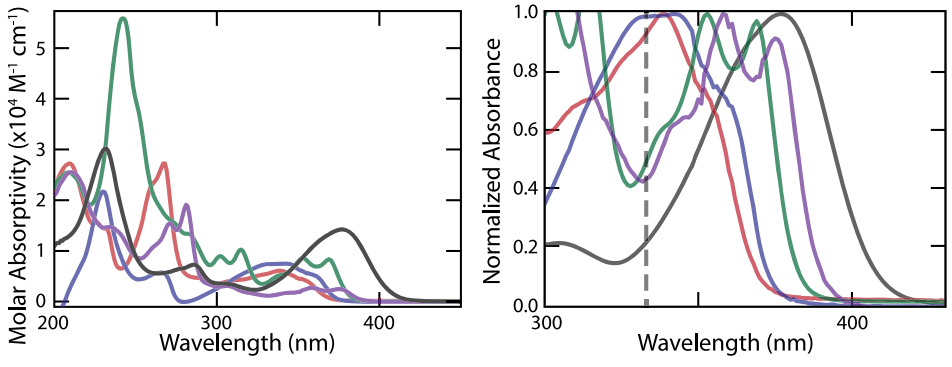

Figure 4. The absorbance spectrum of each molecule was measured in methanol solution at room temperature, at a concentration of ∼10^{-5} M. Spectra are color coded as **1** (black), **2** (red), **3** (blue), **4** (green), and **5** (purple). Spectra were acquired with maximum absorbance below 1.0 to ensure linearity with concentration. The left panel shows the full molar absorptivity spectra, while the right panel shows a normalized version of the lowest-energy absorbance feature of each compound. The dashed, black line in the right panel shows the 327.9 nm peak absorption wavelength for unaltered 2-quinolinone in methanol solution, as reported in the literature.

https://doi.org/10.1021/acs.jpca.1c04560
J. Phys. Chem. A 2021, 125, 9757–9769

progression corresponding to ~1250 cm^{-1} peak spacing, with the higher energy peak having slightly larger relative magnitude. Frequency calculations performed using the structures shown in Figure 3 resulted in several modes with frequencies near 1250 cm^{-1}, for both **4** and **5**. These vibrational modes exhibit characteristic motion consistent with C−C bond stretching in the conjugated rings, along with some rocking of the nearby H atoms. The absorbance spectrum of **5** was red-shifted relative to **4** by ~5 nm, and also absorbed less strongly. Comparing the absorbance spectra of the two sets of closely related structures, molecules **2** and **3** and molecules **4** and **5**, in both cases the stronger-absorbing compound in the pair had a planar ring structure extended away from the nitrogen atom in the lactam ring of the quinolinone, while the weaker absorber extended its rings closer to the nitrogen side of the lactam.

An energy level diagram for each compound at its ground state geometry, generated from DFT calculations, is displayed in Figure 5. The S_0 energy levels are plotted on the energy axis relative to electron detachment, such that the position of the S_0 state represents the vertical electron detachment energy of the corresponding compound. Vertical detachment energies were determined by comparing the energy of neutral singlet state of each compound with the energy of the cation doublet state, with both values calculated at the neutral ground state geometry. The energy of the T_1 excited states were determined through an analogous comparison of the energy of the triplet state to the cation state, again with both values calculated at the neutral ground state geometry. Singlet excited state energies for the neutral compounds were calculated with TDDFT using the same functional and basis set as the ground state optimization. The predicted transition energies from these compounds were then used to plot the S_n excited states above the S_0 state along the energy axis.

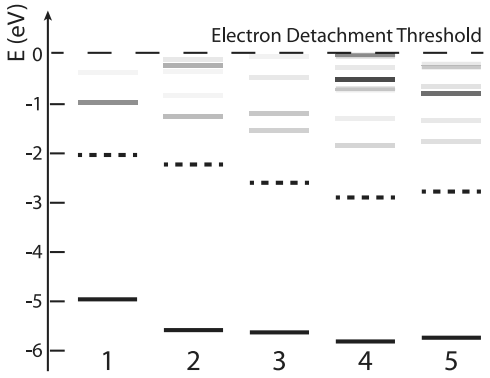

Figure 5. Energy level diagrams for each compound are shown along a common energy axis. All calculations were performed using density functional theory, with the CAM-B3LYP functional and the 6-31G(d,p) basis set. All energies were calculated at the optimized ground state singlet geometry of the neutral compounds. Methanol solvent was included via the polarizable continuum model. The five compounds are labeled along the bottom of the diagram. The lowest energy level shown for each compound is the energy of the optimized singlet ground state, S_0, relative to the electron detachment threshold. For each compound, all singlet excited states, S_n, with energies below the detachment threshold are shown are shown as solid lines. Shading is scaled to the predicted oscillator strength of the corresponding transition, such that darker lines indicate larger oscillator strength. The lowest-energy triplet state of each compound, T_1, is also shown, as a dashed line. No shading variation is employed for the triplet states, since direct optical excitation from the singlet ground state is forbidden.

The diagrams shown Figure 5 demonstrate that all five molecules had similar energy gaps between their singlet ground state, S_0, and their first singlet excited state, S_1. All predicted $S_0 \rightarrow S_1$ transition energies were near 4 eV, corresponding to a predicted excitation wavelength near 310 nm. The predicted transition energies were thus larger than those measured via the absorbance spectra shown in Figure 4, but followed the same pattern. Comparing the observed absorbance spectra to the predicted transitions shown in Figure 5, it was clear that the observed lowest-energy absorption features were most strongly associated with the $S_0 \rightarrow S_1$ transition, especially on the low energy side of the feature. For **1** and **2**, the predicted $S_0 \rightarrow S_2$ transition had a much weaker oscillator strength than the $S_0 \rightarrow S_1$ transition, indicating that photoexcitation should not create significant S_2 population. In **3**, **4**, and **5** the oscillator strength for the $S_0 \rightarrow S_2$ transition was predicted to be comparable to the oscillator strength for the $S_0 \rightarrow S_1$ transition, but the S_2 state was higher in energy by 0.3−0.5 eV. Considering the width of the lowest-energy absorption features of these compounds (see Figure 4), it was not clear if the $S_0 \rightarrow S_2$ transition should have been assigned to higher energy absorption features, or if excitation on the high energy side of the lowest-energy absorbance feature may have excited some S_2 population. For the purpose of analyzing the dynamic measurements reported below, it should be noted that any S_2 population created by excitation of this feature in room temperature, solution phase samples should be expected to relax into the S_1 state within a few hundred femtoseconds.

Compound **1** had the smallest predicted transition energy, and also the most red-shifted absorbance peak. It was also predicted to have a higher ground state energy than the other four compounds, by about 0.5 eV. Compound **1** also had the strongest oscillator strength associated with its S_1 excited state, in agreement with the observation that this compound had the strongest low-energy absorbance feature. It is not yet clear what characteristics of **1** cause it to absorb more strongly than the other compounds studied. Compounds **2**−**5** exhibited similar ground state energies, but different patterns within the singlet excited state manifold. The S_1 states of **2** and **3** were ~0.25 eV higher than the S_1 states of **4** and **5**, consistent with the relatively higher energies and shorter wavelengths of the absorbance features of **2** and **3**. The excited state calculations on compounds **4** and **5** yielded the largest number of singlet excited states below the electron detachment threshold, as well as higher energy singlet excited states with large oscillator strengths that most likely correspond to the strong absorbance features recorded at shorter wavelengths for these compounds. The T_1 excited states, shown in Figure 5 as dashed lines, were ~1 eV lower in energy than the S_1 excited states of each compound.

The excited state calculations also showed that the $S_0 \rightarrow S_1$ transitions were strongly associated with the HOMO → LUMO molecular orbital transitions, which account for >85% of the predicted $S_0 \rightarrow S_1$ transition for all compounds. The electron densities of these molecular orbitals are shown in Figure 6, demonstrating that the electron density involved in the transition was spread across the conjugated, planar region of each molecule. The HOMO → LUMO transitions each showed that excitation creates an additional node in the electron density distribution, a pattern characteristic of $\pi \rightarrow \pi^*$ transitions in conjugated organic molecules. The pendant

https://doi.org/10.1021/acs.jpca.1c04560
J. Phys. Chem. A 2021, 125, 9757−9769

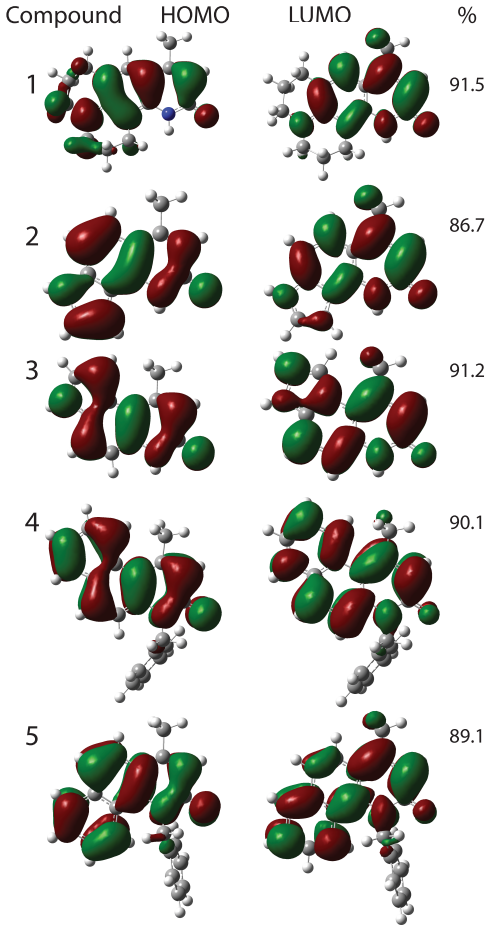

Figure 6. The HOMO and LUMO molecular orbitals for each of the five compounds are shown, with red and green lobes corresponding to opposite phases of the wave function. The percentage contribution of the HOMO → LUMO molecular orbital transition to the predicted S_0 → S_1 transition for each molecule is listed in the right column.

benzyl groups of **4** and **5** did not participate significantly in the predicted HOMO → LUMO transitions. The rotation of the benzyl groups may represent a local energy minimum, rather than a global minimum. No systematic study of the effects of benzyl rotation was performed because these groups do not appear to significantly affect the molecular orbitals shown in Figure 6.

3.2. Emission Spectroscopy. Figure 7 summarizes emission spectroscopy results for compounds **1**−**5**. Each compound was observed to have one emission peak in the range 400−450 nm, with the measured peak emission wavelengths reported in Table 1 as λ_{em}. Table 1 summarizes the key results of static spectroscopy measurements and DFT calculations. The table lists the measured peak absorbance (λ_{abs}) and emission (λ_{em}) wavelengths for each compound, along with the wavelengths corresponding to the calculated energy gaps from the ground state to the lowest lying singlet (λ_{S1}) and triplet (λ_{T1}) excited states and the predicted oscillator strength for S_0 → S_1 excitation (f_{S1}). Additional tables of information from computational results are available in the Supporting Information. Comparing the peak absorption and emission wavelengths reported in Table 1 shows that compounds **1**, **2**, and **3** exhibited markedly larger Stokes shifts than **4** and **5**.

Table 1. Static Spectroscopy and Computational Chemistry Results

compound	λ_{abs} (nm)	λ_{em} (nm)	λ_{S1} (nm)	f_{S1} (unitless)	λ_{T1} (nm)
1	377	445	311	0.4990	424
2	339	409	286	0.2039	369
3	342	427	302	0.2091	409
4	369	409	312	0.1935	425
5	375	419	312	0.1374	418

The TCSPC measurements shown in Figure 7 characterize the fluorescence lifetime of each compound, equivalent to the lifetime of the emitting S_1 excited state. The TCSPC measurements were all well fit by single exponential decays with time constants of up to a few nanoseconds, indicating that the emission is fluorescent rather than phosphorescent. This assignment was supported by the emission spectra, which do

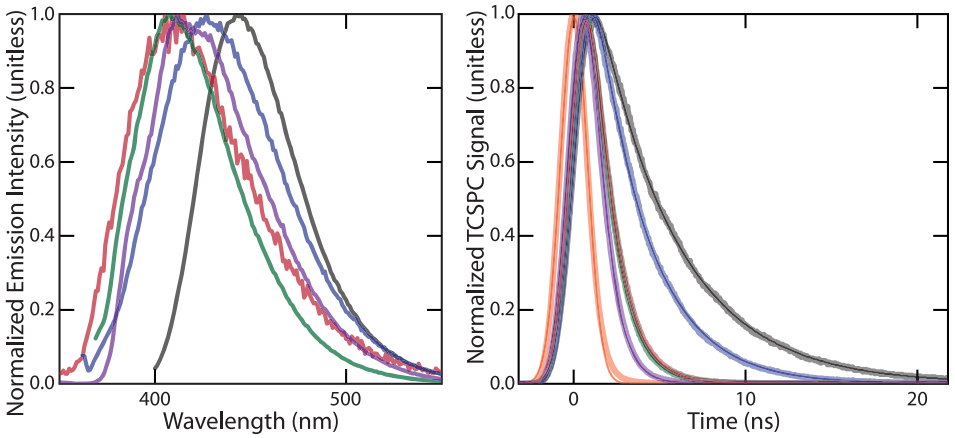

Figure 7. [Left] Normalized emission spectra of all compounds. Spectra are color coded as **1** (black), **2** (red), **3** (blue), **4** (green), and **5** (purple). Spectra were recorded at room temperature in methanol solution, at concentrations on the order of 10^{-5} M. [Right] TCSPC measurements of fluorescence lifetimes are shown for all compounds, using the same color coding scheme as the emission spectra. The instrument response function of the TCSPC measurement is also shown in orange. The thinner, darker lines overlaid on the data show the associated fit functions used to extract fluorescence lifetime values. All measurements were recorded by exciting the room temperature samples in methanol solution at 345 nm, and detecting emission through a 50 nm bandpass filter centered at 450 nm.

https://doi.org/10.1021/acs.jpca.1c04560
J. Phys. Chem. A 2021, 125, 9757−9769

not show any evidence of a second peak or shoulder that could be assigned to phosphorescence. The resulting time constants, corresponding to S_1 lifetimes, are shown as τ_{fl} in Table 2.

Table 2. Dynamic Spectroscopy Results

compound	T_{fl} (ns)	τ_{vib} (ps)
1	4.586 (±0.002)	2.67 (±0.04), 520 (±10)
2	1.2840 (±0.0008)	N/A
3	3.018 (±0.002)	19.3 (±0.1)
4	1.2337 (±0.0008)	27 (±1)
5	0.8493 (±0.0006)	28 (±1)

3.3. Transient Absorption Spectroscopy. The relaxation dynamics of compounds **1**−**5**, subsequent to photoexcitation at 350 nm, were also examined using TA spectroscopy. While each molecule presented unique spectra, the spectral features and dynamic behavior observed were fundamentally similar and could be interpreted using a common model. Figure 8 demonstrates the key spectral and dynamic features of these data sets, as observed in **2**.

Two primary features were observable in the transient spectra of all compounds. The most prominent feature was a large positive peak that increased in amplitude as the time delay between pump and probe laser pulses was increased. In the spectra of compound **2** shown in Figure 8, this feature peaked near 570 nm and was clearly resolved at later time delays. Examining the spectra acquired at various time delays, shown in the right panel of the figure, demonstrates that some positive amplitude existed in this region at early time delays, but a clear peak did not develop until the later time delays. From comparison of spectra acquired at long time delays, it was unclear if the amplitude of this feature was constant or still increasing at the longest time delays, because the changes observed were smaller than the magnitude of the noise. TA data sets for **1**, **4**, and **5** also contained well-resolved, peaked signals with analogous dynamics. Spectra of **3** exhibited positive amplitude at similar wavelengths that followed similar dynamics, but they did not yield a well-resolved peak for this feature even at the longest measured time delays.

The second primary feature observed in all spectra was peakless, positive amplitude at the longest measured wavelengths, which decayed away as the time delay increased. The dynamics of this signal can be most clearly observed in the right panel of Figure 8. The spectra acquired at short time delays contained substantial positive amplitude at wavelengths above 700 nm, which decreased as the time delay between excitation and probe laser pulses increased. This signal was present in the spectra of all five compounds studied, always at the long-wavelength edges of the spectra. No compounds presented a clearly resolved peak, so it is likely this signal was the high energy tail of a peak occurring at longer wavelengths, outside the observed domain.

Other features present in the spectra were less consistently observable across the five compounds studied, or less dynamically interesting. Spectra of all compounds contained coherent artifacts near zero time delay, consisting of broad features with large amplitudes. These features were not analyzed in detail. All spectra also contained increased noise below ∼450 nm, due to variation in the intensity of the probe pulse. The magnitude of this noise increased as wavelength decreased, so wavelengths below 425 nm were excluded from the analysis. Instability in the probe laser pulse also produced a fringed pattern in the high wavelength region of the TA spectra, above ∼700 nm. A similar pattern appeared in the probe laser pulse spectrum, when the ∼800 nm fundamental laser output is slightly overfocused in the sapphire window used to generate the broadband probe beam. Examining kinetic traces at various wavelengths showed that dynamics in this region have a noise level equivalent to other wavelength ranges, despite the observed fringe pattern. The waterfall plot shown in Figure 8 also highlights a region of low amplitude around 475 nm at early time delays. An analogous signal was also observed in the spectra of **1** and **3**, and has negative amplitude for **1**.

The expected kinetic scheme for the observed dynamics is diagrammed in Figure 9c. Excitation at 350 nm should produce a vibrationally excited S_1* state. The 350 nm excitation wavelength overlapped with the lowest energy absorption feature of each compound, which corresponds strongly to the $S_0 \rightarrow S_1$ transition as described above. The 350 nm excitation wavelength falls on the high energy side of the absorption feature for **1**, **4**, and **5**, and near the absorption maximum for **2** and **3**. Varying degrees of vibrational excitation should be expected for each compound. For all compounds, the initially

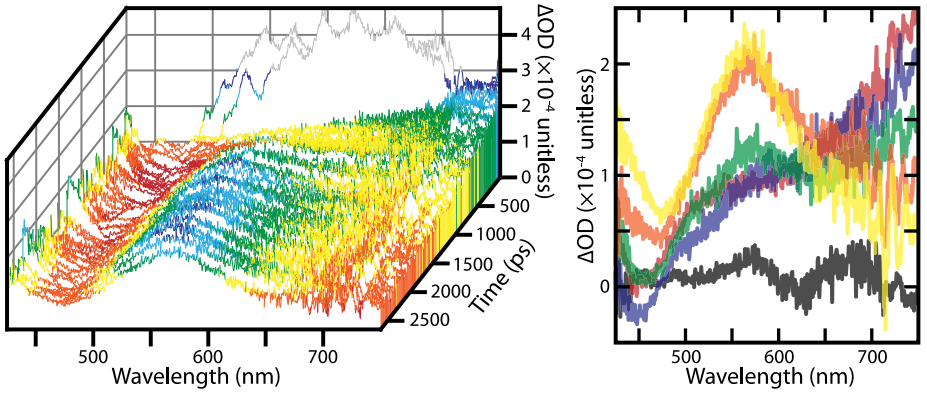

Figure 8. TA spectra of **2** are displayed. Spectra were obtained at room temperature in methanol solution, using an excitation wavelength of 350 nm and a sample with an optical density of ∼0.2. [Left] Waterfall plot of the data, with time increasing from back to front and color coding to emphasize changes in optical density. The color scheme is (all $\times 10^{-4}$): 0−0.5 (red), 0.5−1.0 (orange), 1.0−1.5 (yellow), 1.5−2.0 (green), 2.0−2.5 (cyan), 2.5−3.0 (blue), and >3.0 (gray). [Right] Selected spectra at several time delays, chosen to emphasize key features of the data set. The selected time delays were −506 fs (black), 5.35 ps (red), 52.3 ps (blue), 552 ps (green), 1532 ps (orange), and 2532 ps (yellow).

https://doi.org/10.1021/acs.jpca.1c04560
J. Phys. Chem. A 2021, 125, 9757−9769

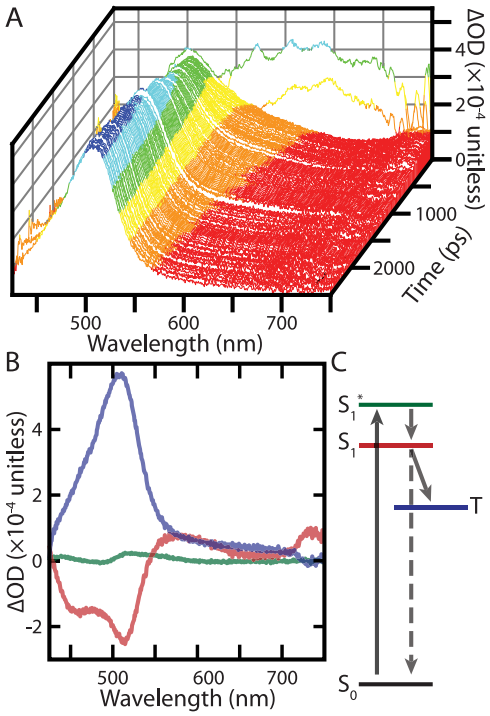

Figure 9. [A] Waterfall plot of TA data for compound **4**, with time increasing from back to front and color coding to emphasize changes in optical density. The color scheme is (all $\times 10^{-4}$): 0−1.0 (red), 1.0−2.0 (orange), 2.0−3.0 (yellow), 3.0−4.0 (green), 4.0−5.0 (cyan), and >5.0 (blue). [B] Decay associated difference spectra resulting from global rate analysis of the data set are shown in part A, using a model with three kinetic components. The time constants associated with the spectra were 27 (±1) ps (green), 1234 ps (red), and 10^{10} ps (blue). The latter two time constants are not reported with error estimates because they were fixed during the fitting procedure. [C] Kinetic scheme used to interpret TA results. The S_1* (green), S_1 (red), and triplet (blue) states have colors matching the corresponding spectra in panel B. Solid arrows represent photoexcitation and relaxation channels included in the global analysis model. A dashed line is used to represent $S_1 \rightarrow S_0$ relaxation channels such as IC and fluorescence, which are not represented in the global analysis model.

formed S_1* population should then relax to the vibrationally relaxed S_1 state on a picosecond time scale. The S_1 population should then decay to the S_0 state by internal conversion (IC) and fluorescence pathways, while some S_1 population should also be converted to a triplet state via intersystem crossing (ISC).

The signals observed in the TA spectra were consistent with this picture. The clearly resolved positive signal at long time delays was assigned as excited state absorption (ESA) by a triplet state on the basis of its long lifetime. Another possible assignment for a feature that does not decay during the observable time domain of ∼2.6 ns would be a photoproduct, but comparison of spectra acquired successively during the experiment demonstrated that this signal did not build up over time as the measurement proceeded. This observation confirms that no permanent, optically active photoproducts were produced, although transient photoproducts could still have been present during the measurements. Further corroboration of the assignment of this feature as triplet ESA is available, because a similar signal was observed in previous TA measurements performed on 7-methoxy-1-methylquinolin-2(1*H*)-one. This signal was assigned as triplet ESA on the basis that its lifetime was reduced from 500 ns under anaerobic conditions to 70 ns in the presence of oxygen.[37]

The positive signal observed at longer wavelengths can be assigned as ESA by the S_1 excited state, again on the basis of its dynamics. The signal grows in quickly at early time delays and decays away over several nanoseconds, as expected for the S_1 population. TDDFT calculations performed at the optimized geometry of the S_1 excited state predict $S_1 \rightarrow S_n$ transitions in the near-infrared for all compounds, so this unpeaked signal could be the high energy tail of an $S_1 \rightarrow S_n$ ESA feature. The $S_1 \rightarrow S_n$ transition energies predicted by TDDFT calculations at the optimized S_1 geometry are available as Supporting Information.

Fitting of kinetic traces corresponding to these two major features produced a set of time constants that were not consistent with the proposed relaxation scheme. The integrated kinetic traces and fitting results are provided in the Supporting Information. Fitting the rise of the triplet ESA feature returned time constants ranging from 700 to 1700 ps, while fitting the decay of the S_1 ESA feature yielded smaller time constants of 440 to 820 ps. These results and further details on the fitting procedure are available as Supporting Information. The S_1 population should decay simultaneously via IC, ISC, and fluorescence. If the time constant for ISC is significantly smaller than the time constant for $S_1 \rightarrow S_0$ relaxation, the branching ratio for generation of triplet population should be large. If the $S_1 \rightarrow S_0$ relaxation pathways have significantly smaller time constants, the branching ratio for triplet formation should be small. In either case, decay of spectral features assigned to the S_1 population should match well with growth of the features caused by the triplet population. The S_1 lifetimes derived from the TA measurement should also agree with those obtained via TCSPC. The lifetimes resulting from fitting kinetic traces were much smaller than the TCSPC-measured lifetimes reported in Table 2, and the growth of signal assigned to triplet ESA had time constants almost twice as large as the time constants for S_1 decay. One possible reason for the observed mismatch between the TA and TCSPC results is the limited time domain observed. The S_1 lifetimes measured via TCSPC were long enough that decay of the S_1 signal should not be complete within the observed time domain of ∼2.6 ns for most compounds. Truncation of the TA data set in this way may have caused the fitted time constants for S_1 population decay to be artificially reduced. Another possible explanation is that overlapping signals in the TA data set may have distorted the fitted time constants.

To address this possibility, global rate analysis was applied to examine the TA spectra in more detail. The number of kinetic components required to be included in the global analysis models to obtain a satisfactory fit of the TA data varied from two to four, depending on the compound. Examination of the residuals associated with each successful model revealed no significant signals not accounted for by the respective model, outside of imperfect modeling of the coherent artifacts at very early time delays. These residuals are available as Supporting Information.

For a given model, each kinetic component included produces one time constant quantifying dynamics in the data set, as well as a decay associated difference spectrum (DADS) and an evolution associated difference spectrum (EADS). The DADS reports the spectrum of fitted amplitudes of the exponential decay associated with the kinetic component,

https://doi.org/10.1021/acs.jpca.1c04560
J. Phys. Chem. A 2021, 125, 9757−9769

while the EADS reports on the changes in the observed transient spectra on the relevant time scale. For this study, the DADS provided the most clearly interpretable signals and are discussed in detail. EADS are available as Supporting Information, but they are not discussed.

Two different modeling strategies were explored. In both strategies, the kinetic component with the longest time constant was constrained to a pseudoinfinite value of 10^{10} ps to match the behavior of the observed long-lived spectral feature, which does not decay within the observed time domain. In one strategy, the time constants for all other kinetic components were unconstrained. In the other strategy, the time constant for a second kinetic component was fixed to the S_1 lifetime value measured via TCSPC. The differences between the results of constrained and unconstrained models were small for all compounds. The DADS for all kinetic components consist of similar features. The time constants for kinetic components other than those fixed as described above were nearly identical for constrained and unconstrained models. The unconstrained models always returned smaller residuals, as expected due to their additional degree of freedom. For **1**, **2**, and **3**, no statistically significant difference between the quality of fit obtained using constrained and unconstrained models was found via an *F*-test at the 95% confidence level. For **4** and **5**, the *F*-test results showed that the differences between constrained and unconstrained models were statistically significant at the 95% confidence level. While the quality of the unconstrained fits was better than the quality of the constrained fits, inspection of residuals from the constrained fits showed that they did not exclude any significant signals. It is likely that the improvement in the unconstrained fits came from a better fit of either the noise in the data set or the coherent artifacts present at early times. The constrained fits, which match well with the expected model for electronic relaxation, are therefore preferred. The DADS for the constrained fit of **4** is shown in Figure 9B, and the constrained fit results for all compounds are discussed in detail. Parameters resulting from unconstrained fits are available as Supporting Information.

Figure 9 shows the TA data for **4**, along with the DADS from the constrained fit and the kinetic scheme used to interpret the data. The green DADS in Figure 9B shows the spectrum of fitted amplitudes for the fastest-decaying kinetic component of the model, assigned to the S_1* population created by photoexcitation. The fitted time constant for this component was 27 (±1) ps for **4**. The DADS showed two peaks at 437 and 525 nm, which were assigned as ESA by the S_1* state because they were positive signals. While the amplitude of these two features was small, including this component in the model did produce a significantly higher quality fit than a model with only two kinetic components. The relative strength of this signal was similar for compound **5**, and it is much stronger in compounds **1** and **3**. For compound **2**, attempting to include an S_1* component in the global analysis model resulted in an unphysical, extremely short time constant. In all cases where the S_1* signal was observed, it consisted of one or more positive peaks assigned as ESA by the S_1* state. The recovered time constant values are reported as τ_{vib} in Table 2.

The red DADS shown in Figure 9B represents the second kinetic component in the model, which corresponds to the vibrationally relaxed S_1 population in the proposed scheme. The DADS shown in the figure exhibited negative signal peaking at 514 nm, with a shoulder at 461 nm. Because the ground state bleach signal was well outside the wavelength range probed in this experiment, the most likely assignment of negative signals is stimulated emission (SE). The observed negative signal overlapped well with the emission spectrum of **4**, which peaked at 409 nm but still exhibited >10% of maximum magnitude at 508 nm, supporting the assignment of SE from the S_1 state. The origin of the two-peak structure found in the DADS is unclear, but may be the result of imperfect modeling due to overlap of the negative S_1 SE signal with the strong T_1 ESA signal. The DADS also contained positive signal at wavelengths above ∼540 nm, which were assigned as ESA by the S_1 population. TDDFT calculations performed at the S_1 geometry predicted transitions at 555 nm ($S_1 \rightarrow S_8$), 598 nm ($S_1 \rightarrow S_7$), and 629 nm ($S_1 \rightarrow S_6$), in reasonable agreement with the observed positive signal.

For all compounds, the DADS associated with the second kinetic component were characterized by negative signal at shorter wavelengths, and positive signal at longer wavelengths. The negative signals overlapped with the emission spectra of the compounds, supporting assignment as SE from the S_1 state. The negative signal in the DADS extended to longer wavelengths than the emission spectrum in all cases. The positive signals at longer wavelengths generally did not exhibit clear peaks, but positive signal in this region was consistent with predicted transitions from TDDFT calculations performed at the S_1 geometry of each compound. These observations support assignment of this kinetic component as signal from the S_1 state. The associated time constants were fixed to the S_1 lifetime values measured via TCSPC, reported as τ_{fl} is Table 2.

The blue DADS in Figure 9B represents the final kinetic component, which was assigned a fixed, pseudoinfinite time constant because the signal observed in the TA data did not decay within the observed time domain. This feature was observed for all five compounds, with the peak wavelength and shape closely matching the long-lived spectral feature in the corresponding TA data set. This feature was assigned as ESA by a triplet state on the basis of its long lifetime, lack of evidence for the formation of photoproducts, and similar previously reported measurements,[37] as discussed above.

Modeling of TA data for **1** also returned a fourth kinetic component. Including this extra component significantly improved the quality of the fit. The DADS associated with this additional component consisted of a negative signal peaking near 450 nm, with a long tail on the high-wavelength side that became slightly positive above 650 nm. This negative peak matched well with the SE signal expected from the S_1 state of **1**, because it overlaps nearly exactly with the static emission peak at 445 nm. The time constant associated with this DADS was 520 (±10) ps. It is likely that **1** shows S_1* vibrational relaxation dynamics on two time scales, corresponding to the two recovered time constants of 2.67 (±0.04) ps and 520 (±10) ps. It is not clear why this should be true for **1** and not for the other four compounds. One possible explanation is that the S_1 absorbance feature of **1** is the most red-shifted, as shown in Figure 4. Excitation at 350 nm may have imparted more vibrational energy to the excited population, opening additional relaxation channels or simply making the observed vibrational relaxation signals stronger.

Several factors may have contributed to imperfect modeling of the TA data, resulting in mismatch between the model results and expected signals. First, exponential decay of the S_1

https://doi.org/10.1021/acs.jpca.1c04560
J. Phys. Chem. A 2021, 125, 9757−9769

Table 3. Estimating Triplet Population Using Transient Absorption Data

compound	λ_T(nm)	$\Delta OD_{>2\ ns}$ ($\times 10^{-4}$unitless)	A_{350} (unitless)	$\Delta OD_{>2ns}/A_{350}$ratio ($\times 10^{-4}$unitless)	relative triplet population (unitless)
1	560	2.45	1.098	2.23	0.37
2	565	2.16	0.880	2.45	0.41
3	560	1.05	0.869	1.21	0.20
4	505	5.33	0.890	5.99	1.00
5	490	2.87	0.727	3.94	0.66

population was incomplete within the observed time domain of the TA data set. Only compound **5**, with the shortest S_1 lifetime, supported fast enough S_1 decay dynamics that the observed time domain was three times larger than the S_1 lifetime. In other compounds, the S_1 lifetimes were too long for decay dynamics to be fully observed. A combination of noise in the data set and lack of data at long time delays may have allowed fits to converge onto incorrect time constants for S_1 decay in unconstrained fits. Second, for all compounds the negative signal in the DADS for the S_1 component overlapped strongly with the positive signal in the DADS of the triplet component. The models therefore must simultaneously fit decaying and growing signals in the same spectral region, which may degrade the quality of the results because such competing dynamics are notoriously difficulty to disentangle. Finally, the sequential decay model requires that all decaying S_1 population be converted to the triplet state, whereas real S_1 population also decays simultaneously to S_0 via IC and fluorescence. Employing a model that included simultaneous decay of S_1 population to both S_0 and T_1 did not produce useful results. More details are available in the Supporting Information. The most likely reason for this ambiguity is the overlap of S_1 and T_1 signals in the data, so in future studies TA measurements with a broader spectral range to further facilitate detailed interpretation and decouple the competing dynamic signals are highly desirable.

Table 2 summarizes the dynamic spectroscopy results for all compounds, listing the fluorescence lifetimes measured by TCSPC (τ_{fl}), and the time scale for vibrational relaxation of S_1* (τ_{vib}) resulting from global analysis of the TA data. As described above, no vibrational relaxation time constant was recovered for **2**, and a second vibrational relaxation channel was present for **1**.

3.4. Analysis. Collectively, the measurements reported here inform on the usefulness of modified 2-quinolinones for various applications, as well as the structure−function relationship observed. Expanding the conjugation network of the molecules was not observed to be an especially effective way to modify their absorbance and emission spectra. While some changes in the shape of the absorbance spectra were observed, along with shifting of absorbance and emission peaks, similar changes have been produced by simpler modifications and substitutions to the 2-quinolinone core.[24−27]

The strong performance of these molecules as antennae in LRET detection schemes is likely due to effective triplet formation, with the triplet excited states formed in the quinolinones then being transferred to the lanthanide ion. These triplet states are also likely to be the primary driver of photocatalytic applications. It has been previously noted that analogous coumarins, which substitute an oxygen atom for the nitrogen found in the lactam ring of 2-quinolinones, do not provide significant triplet yield upon photoexcitation.[37] This observation was explained as being due to an increase in spin−orbit coupling in the quinolinones, caused directly by the presence of the nitrogen atom, although the mechanism by which a nitrogen atom increases spin−orbit coupling remains unclear. Still, triplet formation may be a key driver of utility for 2-quinolinones in applications where they are favored over coumarins.

An estimate of the relative magnitude of the triplet population produced by photoexcitation of each compound at 350 nm was calculated from the TA data. This analysis was based on the TA data itself rather than the global rate analysis results. The average final amplitude of the triplet ESA feature in each TA data set was estimated. To do this, the signal in each TA spectrum was averaged over a 4 nm range at the peak of the triplet ESA feature. For each compound, the average signal amplitude at time delays greater than 2 ns was then determined, yielding a single value for each compound that quantifies the average triplet ESA signal at long times. These average signal amplitudes were then normalized to the absorbance of the TA samples at 350 nm, to account for differences in the amount of light absorbed during photoexcitation. These absorbances were measured in 1 cm cuvettes, prior to the TA experiments. Finally, the normalized, average signals were divided by the largest value in the set, resulting in ratios that estimate the relative triplet population. It should be noted that these are only rough estimates. This method of quantifying the triplet population did not account for possible variations in the oscillator strength of ESA by the T_1 state in different compounds, which would alter the correspondence between the magnitude of the TA signal and the triplet population. The bandwidth and spectral profile of the excitation pulse were also neglected. Additionally, in most data sets the triplet population was still increasing slightly, even at time delays greater than 2 ns. This should result in an underestimation of the triplet population in compounds with longer S_1 lifetimes, such as **1** and **3**. Still, the rough estimates provide a useful framework for discussion of the triplet populations. Results are shown in Table 3. The peak wavelength of the triplet feature is reported as λ_T, the average TA signal at long time delays is reported as $\Delta OD_{>2\ ns}$, and the absorbance of the TA samples at 350 nm is A_{350}.

Compound **4** exhibited the strongest triplet signal in the TA measurements, and the largest relative population in Table 3. The similar compound **5** gave the second largest average triplet ESA signal and relative triplet population. In these two molecules, the quinolinone rings were extended via an additional benzene ring fused to the 2-quinolinone core. They also both contained a pendant benzyl group bound to their nitrogen atom. Additionally, these molecules also had red-shifted absorbance features, meaning that excitation at 350 nm excited the high-energy side of the S_1 absorption feature. This was also the case for **1**, which had a much lower estimated triplet population. Interestingly, **2** and **3** did not have particularly large estimated triplet populations, despite the fact that they contained additional nitrogen atoms in their extended structures. In light of this observation, the

https://doi.org/10.1021/acs.jpca.1c04560
J. Phys. Chem. A 2021, 125, 9757−9769

mechanism for triplet production in quinolinones remains unclear. Adding nitrogen atoms to the structure in compounds **2** and **3** was less effective in promoting triplet production than structural changes in other compounds. The compounds producing the largest relative triplet populations had changes to their conjugated, coplanar moiety and also a pendant benzyl ring attached to their nitrogen atom. It is not yet clear which structural change was more effective in promoting triplet production, or if the changes in triplet population were instead driven by the shifting of the S_1 absorbance feature.

Further mapping of the correspondence between the triplet yield of photoexcitation in 2-quinolinones and their structure is necessary to fully determine the molecular design principles that will maximize triplet production. Additional experiments that can fully disentangle the overlapping S_1 and triplet signals would provide more clarity. Toward this end, TA measurements that capture ground state bleach signal are highly desirable because they should provide a clear signal of recovery of the S_0 population. TA experiments with near-IR detection may also provide a clearer view of S_1 decay dynamics, because TDDFT calculations predict $S_1 \rightarrow S_n$ transitions in this range for all compounds. More detailed characterization of the triplet spectrum by photoinduced absorption spectroscopy may also help clarify interpretation of the TA signals. Coupled with characterization of fluorescence quantum yields, this suite of measurements could potentially allow full quantization of the time constants for fluorescence, ISC, and IC in these molecules. Additionally, the usefulness of the triplet states produced for photocatalytic applications should be characterized. Flash photolysis experiments could provide triplet lifetimes, if they survive on long enough time scales to be observed. The yield of photocatalysis could also be measured directly and compared for various compounds.

4. CONCLUSION

Electronic relaxation dynamics were characterized in a set of 2-quinolinones with expanded ring structures. Extending the ring system was observed to redshift absorbance and emission spectra in a manner consistent with predictions from computational chemistry. Electronic relaxation dynamics were characterized with a combination of TA and TCSPC spectroscopies. For all compounds, the S_1 excited state was formed within a few picoseconds of excitation. Radiative relaxation through fluorescence was observed in all compounds, with fluorescence lifetimes of 5 ns or less. The formation of a triplet state surviving beyond 2.5 ns was observed in all compounds. The largest relative triplet population was observed in compounds that extend the planar, conjugated ring structure of the quinolinone moiety with an additional benzene ring, and also have a benzyl group attached to their nitrogen atom. Further investigation is needed to more completely quantify the rates of various photophysical processes in these compounds, identify chemical modifications that will increase triplet yield, and compare the relative photocatalytic effectiveness of the compounds. Higher triplet yields should improve the functionality of 2-quinolinones in photocatalytic and photochemical applications.

■ ASSOCIATED CONTENT

Supporting Information

The Supporting Information is available free of charge at https://pubs.acs.org/doi/10.1021/acs.jpca.1c04560.

Additional details from density functional theory calculations, further analysis of the vibrational progressions observed in the absorbance spectra of compounds **2**−**5**, and three-dimensional waterfall plots of the transient absorbance spectra of all compounds, complete results from fitting transient absorption signal both directly and via global rate analysis, and complete results from fitting time-correlated single photon counting data (PDF)

■ AUTHOR INFORMATION

Corresponding Author

Graham B. Griffin − *Department of Chemistry and Biochemistry, DePaul University, Chicago, Illinois 60614, United States;* orcid.org/0000-0001-6586-6284; Phone: (773)325-7099; Email: ggriffi6@depaul.edu; Fax: (773)325-7421

Authors

Alana Fligelman − *Department of Chemistry and Biochemistry, DePaul University, Chicago, Illinois 60614, United States*

Gonto Johns − *Department of Chemistry and Biochemistry, DePaul University, Chicago, Illinois 60614, United States*

Christina Guyn − *Department of Chemistry and Biochemistry, DePaul University, Chicago, Illinois 60614, United States*

Alexis Petrauskas − *Department of Chemistry and Biochemistry, DePaul University, Chicago, Illinois 60614, United States*

Paul A. Vadola − *Department of Chemistry and Biochemistry, DePaul University, Chicago, Illinois 60614, United States;* orcid.org/0000-0002-9176-3171

Complete contact information is available at: https://pubs.acs.org/10.1021/acs.jpca.1c04560

Notes

The authors declare no competing financial interest.

■ ACKNOWLEDGMENTS

Acknowledgment is made to the Donors of the Petroleum Research Fund, administered by the American Chemical Society, for support of this research. Use of the Center for Nanoscale Materials, an Office of Science user facility, was supported by the U.S. Department of Energy, Office of Science, Office of Basic Energy Sciences, under Contract No. DE-AC02-06CH11357. This work made use of the shared facilities at the University of Chicago Materials Research Science and Engineering Center, supported by National Science Foundation under award number DMR-2011854. David Gosztola is acknowledged for assistance collecting the transient absorption data. Justin Jureller is acknowledged for assistance collecting the time-correlated single photon counting data. Joris Snellenburg is acknowledged for assistance conducting global analysis of transient absorption data using the Glotaran program.

■ REFERENCES

(1) Burglová, K.; Rylová, G.; Markos, A.; Prichystalova, H.; Soural, M.; Petracek, M.; Medvedikova, M.; Tejral, G.; Sopko, B.; Hradil, P.; et al. Identification of Eukaryotic Translation Elongation Factor 1-α 1 Gamendazole-Binding Site for Binding of 3-Hydroxy-4(1H)-quinolinones as Novel Ligands with Anticancer Activity. *J. Med. Chem.* **2018**, *61* (7), 3027−3036.

(2) Carta, D.; Bortolozzi, R.; Hamel, E.; Basso, G.; Moro, S.; Viola, G.; Ferlin, M. G. Novel 3-Substituted 7-Phenylpyrrolo[3,2-f]quinolin-9(6H)-ones as Single Entities with Multitarget Antiproliferative Activity. *J. Med. Chem.* **2015**, *58* (20), 7991−8010.
(3) di Cagno, M.; Styskala, J.; Hlaváč, J.; Brandl, M.; Bauer-Brandl, A.; Skalko-Basnet, N. Liposomal solubilization of new 3-hydroxyquinolinone derivatives with promising anticancer activity: a screening method to identify maximum incorporation capacity. *J. Liposome Res.* **2011**, *21* (4), 272−278.
(4) Lin, J.; Lu, W.; Caravella, J. A.; Campbell, A. M.; Diebold, R. B.; Ericsson, A.; Fritzen, E.; Gustafson, G. R.; Lancia, D. R.; Shelekhin, T.; et al. Discovery and Optimization of Quinolinone Derivatives as Potent, Selective, and Orally Bioavailable Mutant Isocitrate Dehydrogenase 1 (mIDH1) Inhibitors. *J. Med. Chem.* **2019**, *62* (14), 6575−6596.
(5) Detsi, A.; Bouloumbasi, D.; Prousis, K. C.; Koufaki, M.; Athanasellis, G.; Melagraki, G.; Afantitis, A.; Igglessi-Markopoulou, O.; Kontogiorgis, C.; Hadjipavlou-Litina, D. J. Design and Synthesis of Novel Quinolinone-3-aminoamides and Their α-Lipoic Acid Adducts as Antioxidant and Anti-inflammatory Agents. *J. Med. Chem.* **2007**, *50* (10), 2450−2458.
(6) Duplantier, A. J.; Becker, S. L.; Bohanon, M. J.; Borzilleri, K. A.; Chrunyk, B. A.; Downs, J. T.; Hu, L.-Y.; El-Kattan, A.; James, L. C.; Liu, S.; et al. Discovery, SAR, and Pharmacokinetics of a Novel 3-Hydroxyquinolin-2(1H)-one Series of Potent d-Amino Acid Oxidase (DAAO) Inhibitors. *J. Med. Chem.* **2009**, *52* (11), 3576−3585.
(7) Edwards, J. P.; West, S. J.; Pooley, C. L. F.; Marschke, K. B.; Farmer, L. J.; Jones, T. K. New nonsteroidal androgen receptor modulators based on 4-(trifluoromethyl)-2(1H)-pyrrolidino[3,2-g]-quinolinone. *Bioorg. Med. Chem. Lett.* **1998**, *8* (7), 745−750.
(8) Harrington, P. E.; Croghan, M. D.; Fotsch, C.; Frohn, M.; Lanman, B. A.; Pennington, L. D.; Pickrell, A. J.; Reed, A. B.; Sham, K. K. C.; Tasker, A.; et al. Optimization of a Potent, Orally Active S1P1 Agonist Containing a Quinolinone Core. *ACS Med. Chem. Lett.* **2012**, *3* (1), 74−78.
(9) Oshiro, Y.; Sakurai, Y.; Sato, S.; Kurahashi, N.; Tanaka, T.; Kikuchi, T.; Tottori, K.; Uwahodo, Y.; Miwa, T.; Nishi, T. 3,4-Dihydro-2(1H)-quinolinone as a Novel Antidepressant Drug: Synthesis and Pharmacology of 1-[3-[4-(3-Chlorophenyl)-1-piperazinyl]-propyl]-3,4- dihydro-5-methoxy-2(1H)-quinolinone and Its Derivatives. *J. Med. Chem.* **2000**, *43* (2), 177−189.
(10) Oshiro, Y.; Sato, S.; Kurahashi, N.; Tanaka, T.; Kikuchi, T.; Tottori, K.; Uwahodo, Y.; Nishi, T. Novel Antipsychotic Agents with Dopamine Autoreceptor Agonist Properties: Synthesis and Pharmacology of 7-[4-(4-Phenyl-1-piperazinyl)butoxy]-3,4-dihydro-2(1H)-quinolinone Derivatives. *J. Med. Chem.* **1998**, *41* (5), 658−667.
(11) Aly, A. A.; Ramadan, M.; Abuo-Rahma, G. E.-D. A.; Elshaier, Y. A. M. M.; Elbastawesy, M. A. I.; Brown, A. B.; Bräse, S., Quinolones as prospective drugs: Their syntheses and biological applications. In *Adv. Heterocycl. Chem.*; Academic Press: **2020**.
(12) Badgujar, N. S.; Pazicky, M.; Traar, P.; Terec, A.; Uray, G.; Stadlbauer, W. N-Carboxymethylated 6,7-Dimethoxy-4-trifluoromethylcarbostyrils as Fluorescence Markers for Amino Acids, Peptides, Amino Carbohydrates and Amino Polysaccharides. *Eur. J. Org. Chem.* **2006**, *2006* (12), 2715−2722.
(13) Clima, L.; Bannwarth, W. Building-Block Approach for the Straightforward Incorporation of a New FRET (Fluorescence-Resonance-Energy Transfer) System into Synthetic DNA. *Helv. Chim. Acta* **2008**, *91* (1), 165−175.
(14) Kainmüller, E. K.; Ollé, E. P.; Bannwarth, W. Synthesis of a new pair of fluorescence resonance energy transfer donor and acceptor dyes and its use in a protease assay. *Chem. Commun.* **2005**, *43*, 5459−5461.
(15) Kim, S. H.; Ge, P.; Katzenellenbogen, J. A. A new quinoline sensitizer-centered lanthanide chelate and its use for protein labling on Ni-NTA beads for TR LRET assays. *Chem. Commun.* **2009**, *2*, 183−185.
(16) Kovacs, D.; Mathieu, E.; Kiraev, S. R.; Wells, J. A. L.; Demeyere, E.; Sipos, A.; Borbas, K. E. Coordination Environment-Controlled Photoinduced Electron Transfer Quenching in Luminescent Europium Complexes. *J. Am. Chem. Soc.* **2020**, *142* (30), 13190−13200.
(17) Ganesan, P.; Chandiran, A.; Gao, P.; Rajalingam, R.; Grätzel, M.; Nazeeruddin, M. K. Molecular Engineering of 2-Quinolinone Based Anchoring Groups for Dye-Sensitized Solar Cells. *J. Phys. Chem. C* **2014**, *118* (30), 16896−16903.
(18) Moon, Y.; Jang, E.; Choi, S.; Hong, S. Visible-Light-Photocatalyzed Synthesis of Phenanthridinones and Quinolinones via Direct Oxidative C−H Amidation. *Org. Lett.* **2018**, *20* (1), 240−243.
(19) Wang, C.; Qiao, J.; Liu, X.; Song, H.; Sun, Z.; Chu, W. Visible-Light-Induced Decarboxylation Coupling/Intramolecular Cyclization: A One-Pot Synthesis for 4-Aryl-2-quinolinone Derivatives. *J. Org. Chem.* **2018**, *83* (3), 1422−1430.
(20) Eggeling, C.; Widengren, J.; Rigler, R.; Seidel, C. A. M. Photobleaching of Fluorescent Dyes under Conditions Used for Single-Molecule Detection: Evidence of Two-Step Photolysis. *Anal. Chem.* **1998**, *70* (13), 2651−2659.
(21) Ge, P.; Selvin, P. R. Carbostyril Derivatives as Antenna Molecules for Luminescent Lanthanide Chelates. *Bioconjugate Chem.* **2004**, *15* (5), 1088−1094.
(22) Li, M.; Selvin, P. R. Amine-Reactive Forms of a Luminescent Diethylenetriaminepentaacetic Acid Chelate of Terbium and Europium: Attachment to DNA and Energy Transfer Measurements. *Bioconjugate Chem.* **1997**, *8* (2), 127−132.
(23) Cao, D.; Liu, Z.; Verwilst, P.; Koo, S.; Jangjili, P.; Kim, J. S.; Lin, W. Coumarin-Based Small-Molecule Fluorescent Chemosensors. *Chem. Rev.* **2019**, *119* (18), 10403−10519.
(24) Ahvale, A. B.; Prokopcová, H.; Šefčovičová, J.; Steinschifter, W.; Täubl, A. E.; Uray, G.; Stadlbauer, W. 4-Cyano-6,7-dimethoxycarbostyrils with Solvent- and pH-Independent High Fluorescence Quantum Yields and Emission Maxima. *Eur. J. Org. Chem.* **2008**, *2008* (3), 563−571.
(25) Uray, G.; Niederreiter, K. S.; Belaj, F.; Fabian, W. M. F. Long-Wavelength-Absorbing and -Emitting Carbostyrils with High Fluorescence Quantum Yields. *Helv. Chim. Acta* **1999**, *82* (9), 1408−1417.
(26) Fabian, W. M. F.; Niederreiter, K. S.; Uray, G.; Stadlbauer, W. Substituent effects on absorption and fluorescence spectra of carbostyrils. *J. Mol. Struct.* **1999**, *477* (1), 209−220.
(27) Strohmeier, G. A.; Fabian, W. M. F.; Uray, G. A Combined Experimental and Theoretical Approach toward the Development of Optimized Luminescent Carbostyrils. *Helv. Chim. Acta* **2004**, *87* (1), 215−226.
(28) Kelterer, A.-M.; Uray, G.; Fabian, W. M. F. Rational design of long-wavelength absorbing and emitting carbostyrils aided by time-dependent density functional calculations. *Comput. Theor. Chem.* **2015**, *1055*, 25−32.
(29) Saroja, G.; Sankaran, N. B.; Samanta, A. Photophysical study of two carbostyril dyes: investigation of the possible role of a rotary decay mechanism. *Chem. Phys. Lett.* **1996**, *249* (5), 392−398.
(30) Sinha, R. K.; Kundu, T. Vibronic spectra of jet-cooled 1-methyl-2(1H)-quinolinone studied by Fluorescence spectroscopy and Quantum chemical calculation. *Spectrochim. Acta, Part A* **2020**, *238*, 118426.
(31) Kienzler, A.; Flehr, R.; Kramer, R. A.; Gehne, S.; Kumke, M. U.; Bannwarth, W. Novel Three-Color FRET Tool Box for Advanced Protein and DNA Analysis. *Bioconjugate Chem.* **2011**, *22* (9), 1852−1863.
(32) Altevogt née Kienzler, A.; Flehr, R.; Gehne, S.; Kumke, M. U.; Bannwarth, W. Verification and Biophysical Characterization of a New Three-Color Förster Resonance-Energy-Transfer (FRET) System in DNA. *Helv. Chim. Acta* **2012**, *95* (4), 543−555.
(33) Kovacs, D.; Kocsi, D.; Wells, J. A. L.; Kiraev, S. R.; Borbas, K. E. Electron transfer pathways in photoexcited lanthanide(iii) complexes of picolinate ligands. *Dalton Transactions* **2021**, *50*, 4244.
(34) Kovacs, D.; Phipps, D.; Orthaber, A.; Borbas, K. E. Highly luminescent lanthanide complexes sensitised by tertiary amide-linked

https://doi.org/10.1021/acs.jpca.1c04560
J. Phys. Chem. A 2021, 125, 9757−9769

carbostyril antennae. *Dalton Transactions* **2018**, *47* (31), 10702−10714.
(35) Gehne, S.; Flehr, R.; Altevogt neé Kienzler, A.; Berg, M.; Bannwarth, W.; Kumke, M. U. Dye Dynamics in Three-Color FRET Samples. *J. Phys. Chem. B* **2012**, *116* (35), 10798−10806.
(36) Kovacs, D.; Lu, X.; Mészáros, L. S.; Ott, M.; Andres, J.; Borbas, K. E. Photophysics of Coumarin and Carbostyril-Sensitized Luminescent Lanthanide Complexes: Implications for Complex Design in Multiplex Detection. *J. Am. Chem. Soc.* **2017**, *139* (16), 5756−5767.
(37) Paul, N.; Jiang, M.; Bieniek, N.; Lustres, J. L. P.; Li, Y.; Wollscheid, N.; Buckup, T.; Dreuw, A.; Hampp, N.; Motzkus, M. Substituting Coumarins for Quinolinones: Altering the Cycloreversion Potential Energy Landscape. *J. Phys. Chem. A* **2018**, *122* (38), 7587−7597.
(38) Kim, K.; Choi, H.; Kang, D.; Hong, S. Visible-Light Excitation of Quinolinone-Containing Substrates Enables Divergent Radical Cyclizations. *Org. Lett.* **2019**, *21* (9), 3417−3421.
(39) Kim, I.; Kang, G.; Lee, K.; Park, B.; Kang, D.; Jung, H.; He, Y.-T.; Baik, M.-H.; Hong, S. Site-Selective Functionalization of Pyridinium Derivatives via Visible-Light-Driven Photocatalysis with Quinolinone. *J. Am. Chem. Soc.* **2019**, *141* (23), 9239−9248.
(40) Vacala, T.; Bejcek, L. P.; Williams, C. G.; Williamson, A. C.; Vadola, P. A. Gold-Catalyzed Hydroarylation of N-Aryl Alkynamides for the Synthesis of 2-Quinolinones. *J. Org. Chem.* **2017**, *82* (5), 2558−2569.
(41) van Stokkum, I. H. M.; Larsen, D. S.; van Grondelle, R. Global and target analysis of time-resolved spectra. *Biochim. Biophys. Acta, Bioenerg.* **2004**, *1657* (2), 82−104.
(42) Frisch, M. J.; Trucks, G. W.; Schlegel, H. B.; Scuseria, G. E.; Robb, M. A.; Cheeseman, J. R.; Scalmani, G.; Barone, V.; Petersson, G. A.; Nakatsuji, H.; et al. *Gaussian 16*, Rev. C.01; Gaussian: Wallingford, CT, 2016.

https://doi.org/10.1021/acs.jpca.1c04560
J. Phys. Chem. A 2021, 125, 9757−9769